A New 3D Dirac Nodal-line Semi-metallic Graphene Monolith for Lithium Ion Battery Anode Material

SCHOLARONE™
Manuscripts

A New 3D Dirac Nodal-line Semi-metallic Graphene Monolith for Lithium Ion Battery Anode Material

Jie Liu[1], Xiaoyin Li[1], Qiang Wang[1*], Yoshiyuki Kawazoe[2], and Puru Jena[3]

[1]Center for Applied Physics and Technology, Department of Materials Science and Engineering, HEDPS, BKL-MEMD, College of Engineering, Peking University; Beijing 100871, China
[2]New Industry Creation Hatchery Center, Tohoku University, Sendai, 980-8577, Japan
[3]Department of Physics, Virginia Commonwealth University, Richmond, VA 23284, USA

Abstract

Due to the limited specific capacity of graphite, it is highly desirable to develop new alternatives for high performance lithium ion battery (LIB) anode materials. Motivated by the recent synthesis of three-dimensional (3D) graphene (*Phys. Rev. Lett.*, 2016, **116**, 055501), here we propose a new 3D graphene monolith, termed as HZGM-42. State-of-the-art theoretical calculations uncover that HZGM-42 not only possesses a high thermodynamic stability, anisotropic elasticity and high specific strength, but also exhibits unique electronic band structure with Dirac nodal-lines. Equally important, HZGM-42 shows excellent electrical conductivity and uniformly distributed channels for Li ions to transport with fast kinetics. As compared to the commercially used graphite anode, HZMG-42 possesses a much higher theoretical specific capacity (637.7 mAh/g), much lower energy barrier (0.02 eV) for Li ions diffusion along the one-dimensional channels, and a much smaller volume change（2.4%）during charging and discharging operation. This study expands the family of 3D porous carbon materials with great potential for LIBs.

Introduction

Since the commercialization of lithium ion batteries (LIBs) in the early 1990s, graphite has been used as the standard anode material.[1] However, its limited specific capacity (372 mAh/g), significant volume change (10%), and poor cycling performance at high rate cannot meet the requirements for high-tech applications such as advanced electrical vehicles[2] and stationary energy storage.[3] Hence, anode materials with high storage capacity and high rate capability are highly desirable for the next-generation LIBs. In the last three decades, tremendous efforts have been devoted to the investigation of carbon materials for high-performance anode in LIBs because of their unique advantages, such as availability, low cost, nontoxicity, and good lithium intercalation and de-intercalation reversibility.[4-7] Among various carbon anode materials, porous carbon is of particular interest[7-9] as the open pore structures can lead to high specific surface area with a large amount of storage sites for Li-ions, which are favorable for high-capacity LIB anode.[5, 10] However, currently synthesized porous carbon materials[11-16] have some drawbacks when used as anode materials. Firstly, the conductivity of discovered porous carbon possesses relatively low conductivity. For instance, amorphous porous carbon[11] has low electrical conductivity due to its disordered pores and structural defects. Besides, it is difficult to control the arrangement and size of the pores during the synthesis of conventional porous carbon,[11-13] which is unfavorable for Li-ion transport, resulting in a low rate capability. Thus, a question arises: can we find a 3D carbon material with intrinsic ordered nano-pores as well as high electrical conductivity?

It is well known that graphene exhibits the best electrical conductivity among all of the carbon allotropes. Therefore, a possible way to construct a 3D porous carbon structure with high electrical conductivity is to assemble two-dimensional (2D) graphene sheets into 3D graphene monoliths. As a matter as of fact, in recent years, many efforts have been made to achieve 3D graphene networks.[14-18] For instance, some 3D graphene monoliths have been synthesized by integrating zigzag-edged graphene nanoribbons.[19] These structures are found to possess intrinsic nanopores and their carrier velocity of electrons can reach $\sim 10^6$ m s^{-1},[20] indicating that these structures may have good potential as anode materials for LIBs. Inspired by these experimental works, we propose a new 3D graphene monolith, named as HZGM-42. We found that HZGM-42 possesses suitable pore size for favorable Li adsorption, high electrical conductivity, well-organized channels for fast Li ion diffusion, and small volume change during charging and discharging operation. These features are highly desirable for LIB anode materials. This work sheds light on design of new materials with high capacity, rate capability and excellent stability for LIBs.

Computational methods

First-principles calculations are performed within the framework of density functional theory (DFT) implemented in Vienna *Ab initio* Simulation Package (VASP)[21] with the exchange-correlation functional in the Perdew-Burke-Enzerhof (PBE) form.[22] Projector augmented wave (PAW) method[23] is used to treat the interactions between ion cores and valence electrons. The plane-wave cutoff energy for the wave function is set to 500 eV. The Heyd-Scuseria-Ernzerhof (HSE06) hybrid functional[24] is used for

accurate calculations of the electronic structure. For geometry relaxations, the convergence thresholds are set to 10^{-4} eV and 10^{-3} eV/Å for total energy and force component, respectively. The first Brillouin zone is represented by K points sampled using the Monkhorst-Pack scheme[25] with a grid density of $2\pi \times 0.02$ Å^{-1}. *Ab initio* molecular dynamics (AIMD) simulations are performed using the canonical ensemble (NVT) with the Nosé thermostat[26] to examine thermal stability. The calculations of phonon dispersions are carried out by using the linear response method within the density functional perturbation theory[27] as implemented in the Phonopy code.[28] The diffusion barriers of Li ions are calculated by using the climbing-image nudged elastic band (CI-NEB) method[29, 30] as implemented in the VASP transition state tools. The effect of van der Waals interactions is taken into account to investigate Li adsorption and diffusion by using semi-empirical long-range dispersion correction (the PBE-D2 functional),[31] which is essential to account for the long-range electrostatic interactions between Li atoms at high concentrations.[32-34]

Results and discussion

Geometric structure

The optimized crystal structure of the new 3D graphene monolith proposed in this work is presented in Fig. 1a, which is constructed by integrating zigzag graphene nanoribbons with tetrahedrally coordinated carbon chains as cross linkers. This structure possesses a hexagonal primitive cell containing 42 carbon atoms. Hence, we refer to it as hexagonal zigzag graphene monolith (HZGM), named HZGM-42. In this primitive cell, there are four chemically nonequivalent carbon atoms: 6*g* (0, 0.47, 0.25), 12*j* (0.08, 0.46, 0.25),

12j (0.12, 0.45, 0.75), and 12j (0.20, 0.45, 0.75). The 6g atoms form a sp^3-hybridized

carbon chain, whereas the remaining sp^2-hybridized carbons form the zigzag graphene

nanoribbons. Owing to its unique porous configuration, HZGM-42 has a low density of

1.39 g/cm^3, close to that of nanotube bundles (1.33 g/cm^3),[35] and lower than that of

fullerene solid (1.65 g/cm^3).[18] We also calculate the equilibrium density for some other

3D carbon crystals for comparison. The results are summarized in Table 1, which shows

that HZGM-42 has the lowest equilibrium density among those 3D carbon allotropes.

The pores of HZGM-42 could accommodate other atoms or molecules for further

functionalization as is the case 3D carbon-nanotube polymers.[16]

　　To study the effect of van der Waals (vdW) interaction on the geometry of HZGM-42,

we recalculate the lattice parameters with semiempirical vdW correction.[31] For

comparison, the calculations for diamond and graphite are also carried out. The results are

presented in Table S1 in the electronic supplementary information (ESI). We find that the

lattice parameters with and without the semiempirical vdW correction are almost the

same, suggesting that the effect of vdW interaction on the geometry of Hex-C$_{18}$ is weak

and negligible due to the strong covalent bonding. Therefore, the following calculations

of the thermodynamic and mechanical, and electronic properties of HZGM-42 are carried

out using the standard PBE exchange-correlation functional, without vdW corrections.
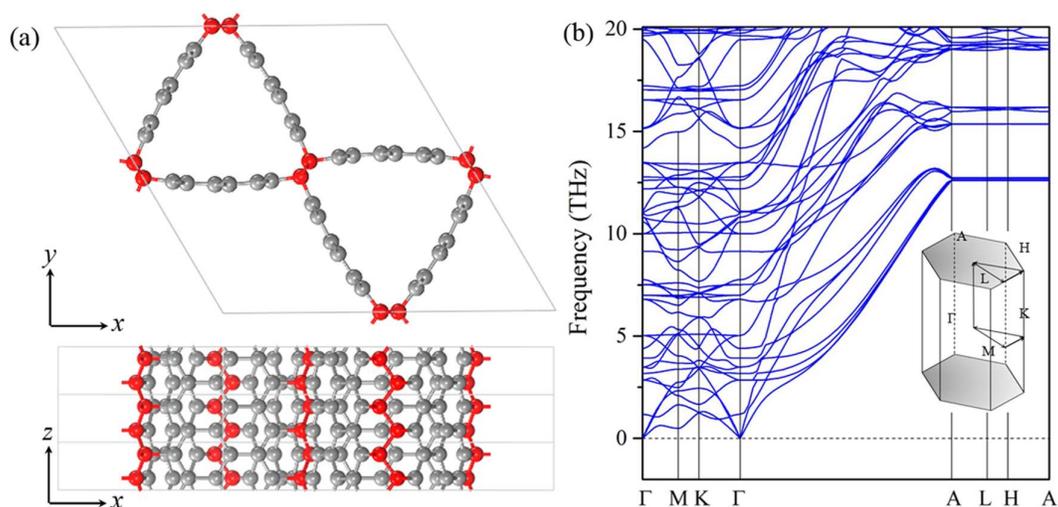
Fig. 1 (a) Top and side views of the optimized geometry structure, and (b) phonon band structure of HAGM-42. The inset in (b) shows the first Brillouin zone and the high symmetry k point path. The light gray and red spheres represent the sp^2- and sp^3-hybridized carbon atoms, respectively.

Table 1 The space group, lattice constants, calculated equilibrium density (ρ in g·cm^{-3}), and the total energy (E_{tot} in eV/atom) of HZGM-42 and some other 3D carbon allotropes.

3D crystal	Space group	Lattice constants (a, b, c)	ρ	E_{tot}
HZGM-42	$P6_3/mcm$	16.82, 16.82, 2.47	1.39	-9.09
graphite	$P6/mmm$	2.46, 2.46, 7.32	2.24	-9.21
diamond	$Fd\bar{3}m$	4.34, 4.34, 4.34	3.62	-9.09
T6	$P4_2/mmc$	2.60, 2.60, 6.00	3.06	-8.64
bct-C$_4$	$I4/mmm$	4.38, 4.38, 2.51	3.42	-8.89
IGN	$Cmcm$	4.33, 4.33, 2.47	2.59	-8.98
bco-C$_{16}$	$Imma$	7.80, 4.90, 3.26	2.57	-8.82
Hex-C$_{18}$	$P6_3/mcm$	8.36, 8.36, 2.46	2.41	-8.96

Energetic stability

To investigate the thermodynamic stability of HZGM-42, we calculate its total energy as a function of volume. For comparison, we also perform calculations of some other 3D carbon crystals, including graphite, diamond, and the recently reported 3D carbon phases, such as T6,[36-38] bct-C_4,[39-41] IGN,[18, 42, 43] bco-C_{16},[44] and Hex-C_{18}.[45] The results are plotted in Fig. S1. We find that HZGM-42 possesses satisfactory thermodynamic stability as its total energy per atom is close to that of diamond, the energy difference between HZMG-42 and graphite is only 0.12 eV/atom, and is energetically favorable over most of the identified 3D metastable carbon phases including T6, bct-C_4, IGN, bco-C_{16}, and Hex-C_{18}. To understand the origin of the high energetic stability of HZMG-42, we analyze its bonding features. The calculated bond length of the sp^2-sp^2 C-C bond for the nanoribbon motif is in the range of 1.42-1.44 Å. For the sp^3-sp^3 C-C bond in the cross linkers of sp^3-hybridized carbon chains, the calculated bond length is 1.52 Å. The average bond angle of the sp^2-hybridized carbon atoms is 119.9°, while that of the sp^3-hybridized carbon atoms is 110.0°. The values of bond lengths and angles for the sp^2- and sp^3- hybridized carbon atoms in HZGM-42 are very close to those of the ideal values of graphite (1.42 Å, 120°) and diamond (1.53 Å, 109.5°), thus leading to the high energetic stability.

Dynamic and thermal Stability

To examine the dynamic stability of HZGM-42, we first calculate its phonon band structure. As shown in Fig. 1b, the absence of imaginary modes in the entire Brillouin zone confirms that HZGM-42 is dynamically stable. More interestingly, we note the

strong anisotropy of the phonon dispersions. Compared the acoustic branches and optical branches along the Γ-M and Γ-K paths with those along the Γ-A, the acoustic branches and most of the optical branches along the Γ-A path show respectively larger slopes, indicating that the group velocities of phonons along the z direction is higher than those along the directions inside the xy plane. We then perform the AIMD simulations to verify the thermal stability of HZGM-42 by increasing temperature from 400 K to 1200 K. We use the 1×1×4 supercell to reduce the constraint associated with periodic boundary condition. The results of simulation at temperature 1200 K are plotted in Fig. S2 in the ESI. These clearly show that the structural skeleton of HZGM-42 remains almost intact after heating for 8 picosecond (*ps*) with a time step of 1 femtosecond (*fs*), and the average value of the total potential energy remains almost constant during the entire simulation, confirming that HZGM-42 is thermally stable, and can withstand temperatures as high as 1200 K.

Mechanical properties

To study the mechanical properties of HZGM-42, we calculate its elastic constants and Young's moduli, and find that HZGM-42 possesses highly anisotropic mechanical properties due to its unique geometric configuration. The elastic constants (C_{33}) and the Young's modulus of the HZGM-42 along the z direction are much larger than those along the x- and y-directions. For comparison, we also calculate the elastic constants and Young's moduli for the recently reported 3D graphene-based architectures, C-honeycomb-28 and C-honeycomb-52 that exhibit superb specific strength along the z direction.[46] The calculated results are given in Table 2. We note that the elastic

constants and the Young's modulus along the z direction of HZGM-42 are even larger than the values of C-honeycomb-28 and C-honeycomb-52, indicating that HZGM-42 possesses an ultrahigh specific strength along the z direction.

To get further understanding of the mechanical strength of the HZGM-42, we also calculate the ideal tensile strength, i.e. the maximum stress required for breaking a perfect crystal.[47] In the calculations of the ideal tensile strength, the quasi-static displacement-controlled deformation is used by imposing the deformation with a small strain increment (a typical value of 0.01 is used) along different directions. The stress-strain curves of HZGM-42, C-honeycomb-28, and C-honeycomb-52 subjected to the tensile stresses along the x, y and z directions are displayed in Fig. 2. In contrast to the nonlinear stress-strain response of C-honeycomb-28 and C-honeycomb -52 along the x and y directions, HZGM-42 exhibits nearly linear stress-strain response along two directions when the strain is less than 0.15, indicating that HZGM-42 is more resistant to tensile stress than C-honeycomb-28 and -52 at the initial strained stage. This linear elasticity of HZMG-42 under tensile loading along the x and y directions is a result of the strongly coupled tension and small bending deformation of the components of zigzag graphene nanoribbon. The ideal tensile strength of HZGM-42 along the z direction is 71.9 GPa, which is higher than the values of C-honeycomb-28 (70.3 GPa) and C-honeycomb-52 (40.1 GPa), confirming its high specific strength along the z direction. The high specific strength of HZGM-42 along the z direction is attributed to the high in-plane strength of the zigzag graphene nanoribbons in the 3D graphene monolith, which is reminiscent of the 3D graphene monoliths assembled by zigzag graphene

nanoribbons with high specific strength along the extend direction of zigzag graphene

motifs reported by Jiang et al..[18]
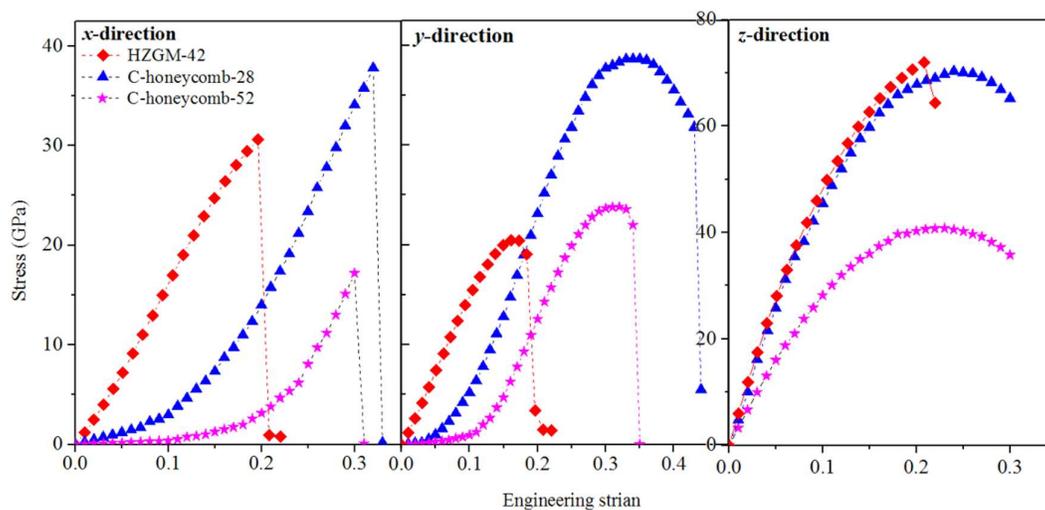
Fig. 2 Orientation-dependent stress-strain relationships for the tensile deformations of HZGM-42, C-honeycomb-28, and C-honeycomb-52.

Table 2 Calculated elastic constants (C_{ij} in GPa), Young's moduli ($Y_{x/y/z}$ in GPa), and ideal tensile strengths ($T_{x/y/z}$ in GPa) of the 3D graphene monoliths including HZGM-42, C-honeycomb-28, and C-honeycomb-52.

|	HZGM-42	C-honeycomb-28	C-honeycomb-52
C_{11}	198.0	163.2	95.1
C_{33}	637.7	581.3	365.0
C_{44}	138.4	100.0	67.7
C_{12}	86.5	152.4	92.7
C_{13}	56.3	38.5	32.3
Y_x	240.4	20.8	4.7
Y_y	240.4	20.8	4.7
Y_z	646.7	571.9	353.9
T_x	30.6	37.8	17.2

T_y	20.5	38.6	23.4
T_z	71.9	70.3	41.0

Electronic properties

To probe the electronic properties of HZGM-42, we calculate its band structure using the PBE functional. As shown in Fig. 3a, HZGM-42 is a semimetal with a Dirac linear dispersion and zero density of states (DOS) near the Fermi level, inheriting the unique electronic property of graphene. The valence and conduction bands along the high symmetry K path Γ-A belong to two different irreducible representations B_1 and B_2, as shown in Fig. 3a, resulting in the unavoidable band crossing. The irreducible representation of an energy state describes the symmetries of its wave vector and wave function under symmetry operations subject to certain point group. We calculate the charge density of states at the points (P1 and P2) close to the crossing point, as shown in Fig. S3a, because the square modulus of the wave function is proportional to the charge density. The difference of charge density between these two states is plotted in Fig. S3b and S3c, which confirms our conclusion that the two bands belong to two different irreducible representations. The band crossing point is located exactly at the Fermi level and is protected by the coexistence of time reversal and space inversion symmetries in HZGM-42 in the absence of the spin-orbit coupling (SOC). Detailed illustration of the relationship between the band crossing point and time reversal and space inversion symmetries is given in Text S1, Fig. S4 and Fig. S5 in the ESI. To confirm the results obtained by the PBE functional, the band structure of HZGM-42 is recalculated using the HSE06 functional, which is known to provide more accurate band structure as the

electron Coulomb screening is more accurately treated in the exchange-correlation energy of electrons in solids.[24] The results plotted in Fig. S6 in the ESI show that the semimetallic feature of HZGM-42 is well preserved at the HSE06 level, suggesting semimetallicity is the intrinsic property of HZGM-42.
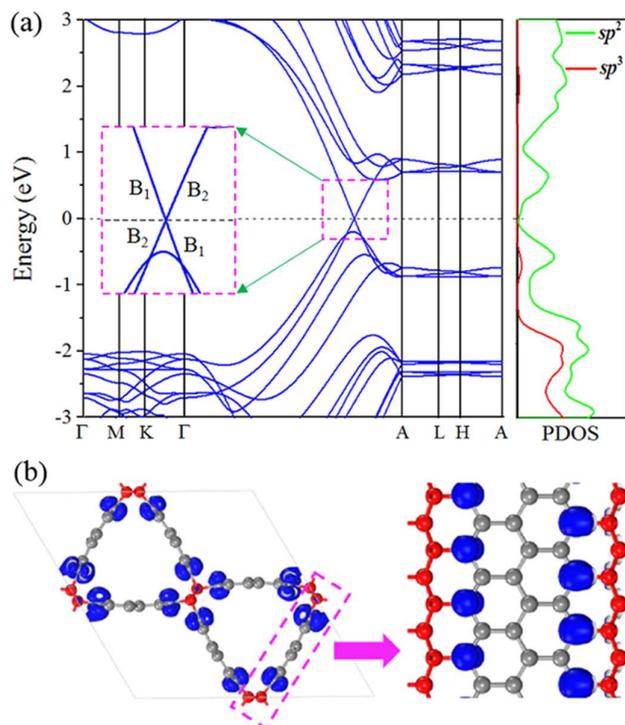

Fig. 3 (a) Electronic band structure and projected DOS of the sp^2-hybridized and sp^3-hybridized carbon atoms. (b) Charge density iso-surface (0.04 e/Å^3) of the valence bands and conduction bands near the fermi level.

The partial DOS projected onto the sp^2- and sp^3- hybridized carbon atoms are also displayed in Fig. 3a. It reveals that the dominant contribution to the DOS around the Fermi level comes from the sp^2-hybridized carbon atoms. To further understand the origin of semimetallicity in this new phase, the band-decomposed charge density is calculated to visualize the charge distribution in the bands near the Fermi level, i.e. the

79th to 90th bands including the six occupied bands and six unoccupied bands. As displayed in Fig. 3b, we find that the main contribution to the charge distribution comes from the sp^2-hybridized carbon atoms, which was bound to the sp^3-hybridized carbon chains.

A further analysis of the band structure of HZGM-42 in the whole Brillouin zone indicates that the band crossing points of the valence and conduction bands form nodal-lines traversing the Brillouin zone. Fig. 4 shows the 3D band structure and band gap contour of HZGM-42 in the mirror invariant planes (100) and (110). One can see that the valence and conduction bands cross along the continuous nodal-lines for both planes, characterizing HZGM-42 as a Dirac nodal-line semimetal. However, a band gap may be opened up at the band crossing points by considering SOC for semi-metallic carbon structures.[44] For the case of HZGM-42, the band gap opened up by the SOC is calculated to be 1.23 meV, which is negligibly weak, suggesting that the semi-matallicity of HZGM-42 is not altered by the SOC.[44] To elucidate the topological feature of HZGM-42, we calculate its Z_2 indices following a commonly used method to identify the topology of Dirac nodal-line states.[48-50] The parities at the eight time-reversal invariant momenta (TRIM) points are -1 (Γ), -1 (3×M), 1 (A), and 1 (3×L), respectively. Then, we obtain the Z_2 indices as (0; 0 0 0), indicating the topological trivial nature of HZGM-42.
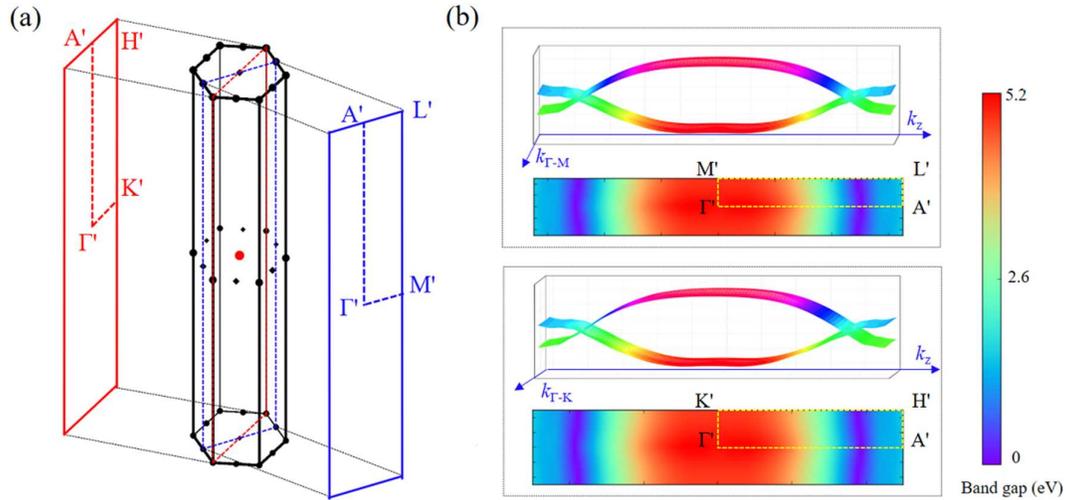
Fig. 4 (a) Bulk Brillouin zone of HZGM-42 with mirror invariant planes (100) indicated by the blue rectangle and (110) indicated by the red rectangle, respectively. (b) 3D band structure (VB and CB) and band gap contour of the two mirror invariant planes. The color bar indicates the band gap at each k point.

Although HZGM-42 is topologically trivial, its Dirac nodal-line band structure provides great promise for high-speed electronic devices. Due to its unique configuration, HZGM-42 exhibits highly anisotropic electrical transport properties. The extended direction of the sp^3 zigzag chains for HZGM-42 in the real space (z direction) corresponds to the Γ-A direction in the reciprocal space. As shown in Fig. 3a, the electronic bands near the Fermi level along the Γ-A direction exhibit large dispersion, indicating that the carriers moving along the z direction have small effective masses. The carrier velocity can be calculated by using the formula $\vec{v}_{\vec{k}} = \hbar \frac{d\mathcal{E}_{\vec{k}}}{d\vec{k}}$ ($\mathcal{E}_{\vec{k}}$ is the energy and $\vec{k}$ is the wavevector). As a benchmark, we first calculate the velocity of Dirac electrons in graphite. The calculated result of 0.87×10^6 m s^{-1} is in good agreement with the value 0.86×10^6 m s^{-1} obtained by Liu et al.,[41] confirming the validity of our calculations. Based on the band structure obtained at the PBE level, the

highest carrier velocity of HZGM-42 along the *z* direction is calculated to be 0.82×10^6 m s^{-1}, which is comparable to the calculated value of Dirac electrons in graphene $(0.87 \times 10^6$ m s$^{-1})$. However, the electronic bands along the paths of A-L, L-H, and A-H in the Brillouin zone are much flatter than those along the Γ-A path, suggesting that carriers move much slower in the *xy* plane than that along the *z* direction. The highly anisotropic transport properties of HZGM-42 may have potential applications in direction-dependent microelectronic devices.[51]

Application as an anode material for LIBs

Due to its regular porousity and intrinsic semi-metallicity, HZGM-42 can provide the basis for the storage and transport of Li ions with good conductivity, making it possible as an anode material for LIBs. Hence, we systematically study its binding and diffusion behavior, therotical capacity, and cycling stability.

We first investigate the binding of a single Li atom into HZGM-42. To avoid the interaction between Li atoms, we adopt a $1 \times 1 \times 4$ supercell. Four possible adsorption sites for Li atom with high geometric symmetry are considered, marked as Li_I, Li_{II}, Li_{III}, and Li_{IV} in Fig. 5. Li_I is the triangle hollow site, Li_{II} is the center site of the "groove" formed by the 8-membered carbon rings, Li_{III} is the site on the top of the 6-membered carbon rings, and Li_{VI} is the edge site of the "groove" formed by the 8-membered carbon rings. To check the strength of Li binding on the three stable sites, we calculate the Li binding energy (E_b), which is defined as

$$E_b = (E_{Li_x\text{-HZGM-42}} - E_{\text{HZGM-42}} - x\mu_{Li})/x, \qquad (1)$$

where $E_{Li_x\text{-HZGM-42}}/E_{\text{HZGM-42}}$ is the total energy of the system with/without Li, and μ_{Li} is the energy of one Li atom in Li bulk.[34] After full optimizations, Li_I, Li_{II}, and Li_{III} are found to be the stable adsorption sites with the binding energies of -0.89, -0.66, and -0.39 eV, respectively, indicating that the most favorable adsorption site for Li atom is the triangular hollow site. Li_{IV} is optimized to Li_{II}. The Bader charge analysis[52] reveals that each Li atom transfers 0.89 electrons to the neighboring C atoms when Li is adsorbed on the Li_I site. For Li_{II} and Li_{III} sites, the transferred charges are found to be 0.88 and 0.90 electrons, respectively. The electron transfers suggest that all the Li atoms in these three adsorption sites donate most of their valance electrons and become Li ions, leading to a strong Coulomb repulsion between the adsorbed Li ions, thus preventing them from clustering.
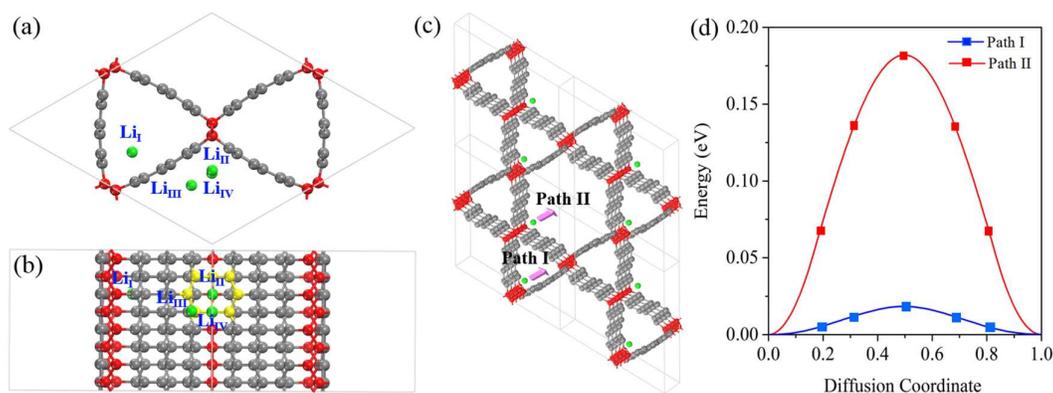
Fig. 5 (a) Top and (b) side views of the possible Li-ion absorption sites. The green, light gray, and red spheres represent Li, sp^2-, and sp^3-hybridized carbon atoms, respectively. The 8-membered carbon ring is marked in yellow. (c) Two migration paths of Li diffusion considered along the z direction in the triangular hollow channel and the hexagonal hollow channel, respectively. (d) The diffusion energy barrier profiles of the two diffusion paths given in (c).

We next calculate the energy barrier for Li ion diffusion. Because the energy barrier

for Li atom to diffuse through the six-membered carbon rings reaches up to 10 eV,[53] the

diffusion along the xy plane in HZGM-42 is, thus, kinetically prohibited. Therefore, we

here only consider diffusion paths along the z direction. Considering the structural

symmetry of HZGM-42 and the preferable Li binding sites, we select two representative

diffusion pathways, as shown in Fig. 5c. Path I is along the *z* direction of the triangular

hollow channel, while path II is along the *z* direction of the hexagonal hollow channel.

Based on climbing-image nudge elastic band (CI-NEB) calculations,[29] the energy

profiles along path I and II are calculated and displayed in Fig. 5d. The calculated

diffusion barriers for path I and II are 0.02 and 0.18 eV, respectively. Both of these are

much lower than the diffusion barrier of Li-ion in graphite (0.22-0.40 eV),[54, 55]

indicating that Li ions can easily diffuse along the two channels. The remarkable 1D

Li-ion diffusion paths with low diffusion barriers suggest that HZGM-42 possesses

high-rate capability as anode material for LIBs. To investigate the effect of point defect

on the 1D diffusion barriers in HZGM-42, we create a mono-vacancy at the sp^3 carbon

site in the $1 \times 1 \times 4$ supercell (see Fig. S7), and calculate the symmetry-inequivalent

migration paths along the z direction around the defect, as displayed in Fig. S8. We find

that for the migration paths in the hexagonal hollow, the diffusion barriers of Path A

and B are 0.49 eV and 0.23 eV, respectively, which are larger than the value of path II

(0.18 eV) in the defect-free structure. For the migration path in the triangular hollow,

the diffusion barrier increases dramatically from 0.02 eV (path I) to 0.26 eV (path C)

when introducing the mono-vacancy of sp^3 carbon atom, suggesting that the defect can

create a potential trap in the defective region, making the diffusion unfavorable.

Therefore, it is necessary to avoid the formation of defects in HZGM-42 when used as an anode material in LIBs. Actually, defects can also trap the metal ion even in layered materials.

We next study the maximum Li capacity of HZGM-42 by increasing Li concentration until the full Li-intercalated configuration is reached, as shown in Fig. S9 in the ESI. According to our definition of binding energy in Eq. (1), a more negative binding energy means a more favorable exothermic reaction between Li and HZGM-42. The corresponding average binding energy E_b is calculated to be -0.19 eV, which is larger than that of Hex-C_{18} (-0.42 eV),[45] but lower than that of $Ti_3C_2(OH)_2$ monolayer ($TiS_3C_2(OH)_2Li_{0.5}$: -0.14 eV)[33] (J. Am. Chem. Soc., 2012, 134, 16909-16916) calculated at the same level. This suggests that Li atoms adsorbed in HZGM-42 are stable, and the phase separation problem is safely avoided at such a high Li concentration. The corresponding theoretical specific capacity of HZGM-42 is 637.71 mAh/g, which is 1.7 times larger than that of graphite, and larger than the values of recently predicated 3D carbon allotropes, such as bco-C_{16}[4], hex-C_{18}.[45] and IGN.[56]

Open-circuit voltage (OCV) is one of the key factors to characterize battery performance under different conditions. It varies with the Li concentration. In general electrode testing, the charge/discharge process of HZGM-42 follows the common half-cell reaction versus Li/Li$^+$:

$$(x_1 - x_2)Li^+ + (x_2 - x_1)e^- + Li_{x_1}\text{-}HZGM\text{-}42 \leftrightarrow Li_{x_2}\text{-}HZGM\text{-}42. \quad (2)$$

Without considering the effects of volume, pressure, and entropy, the average voltage of Li_x-HZGM-42 in the concentration range of $x_1 < x < x_2$ can be estimated using the

following formula:

$$V \approx \frac{E_{Li_{x_1}\text{-}HZGM\text{-}42} - E_{Li_{x_2}\text{-}HZGM\text{-}42} + (x_1 - x_2)E_{Li}}{(x_2 - x_1)},\tag{3}$$

where $E_{Li_{x_1}\text{-}HZGM\text{-}42}$, $E_{Li_{x_2}\text{-}HZGM\text{-}42}$, and E_{Li} are the total energy of Li_{x_1}-HZGM-42, Li_{x_2}-HZGM-42, and Li in its bulk phase, respectively.

To calculate $E_{Li_x\text{-}HZGM\text{-}42}$, we examine 20 symmetry-inequivalent adsorption configurations and select the one with the lowest binding energy for each Li concentration ($Li_xC_{3.5}$: x=0.17, 0.33, 0.50, 0.67, 0.83). The calculated results are plotted in Fig. 6a. The corresponding voltage profile is further calculated and displayed in Fig. 6b. One can see that there are three prominent voltage regions: the plateau region corresponding to a weak interaction between Li ions at the low Li concentration ($0 < x < 0.50$), the plateau region with increasing repulsive interaction in the medium Li concentration ($0.50 < x < 0.83$), and the region with strong repulsive interaction between Li ions at high Li concentration ($0.83 < x < 1.00$). The voltage profile decreases to -0.12 V when Li concentration increases to 0.67, suggesting that the reversible capacity of HZGM-42 as the half-cell is 425.14 mAh/g ($LiC_{5.25}$), which is 66.7% of the maximum Li capacity, larger than that of graphite (372 mAh/g) and IGN (298 mAh/g).[56] By numerically averaging the voltage profile in the region of $0 < x < 0.67$, the average voltage of HZGM-42 is calculated to be 0.50 V that is larger than that of graphite (0.11 V)[32] and bco-C_{16} (0.23 V),[4] but smaller than that of IGN,[56] MoC_2,[57] 2D VS_2 (0.93)[32] and TiO_2 (1.5-1.8).[58, 59] Note: the above results are all based on the half-cell reaction. When connected to cathode as a full-cell, external voltage can overcome the repulsive interaction between Li ions at high concentration, and display a high capacity

(LiC$_{3.5}$: 637.71 mAh/g) and a low average voltage of 0.19 V.
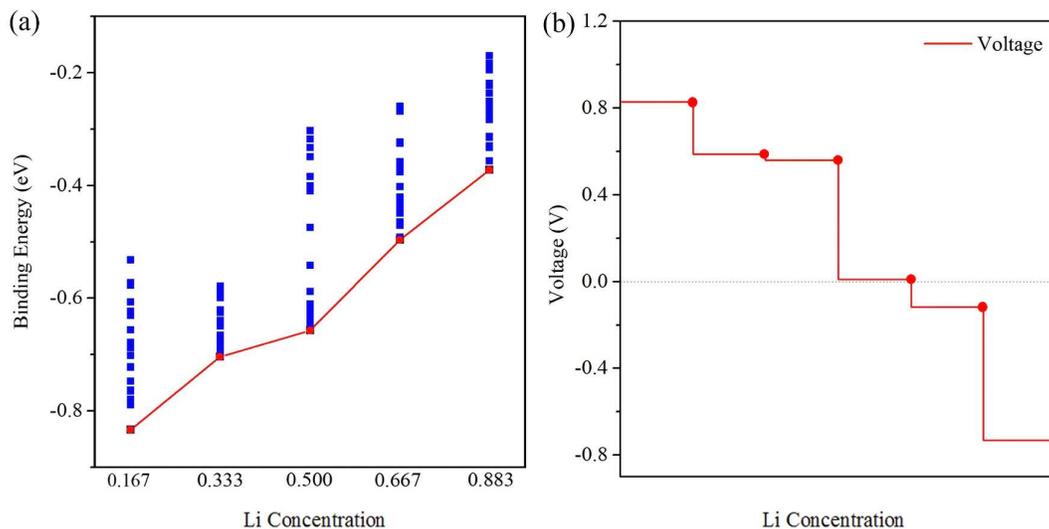
Fig. 6 (a) Binding energies of the 100 configurations for five different Li concentrations. The stable configurations with the lowest energies for each Li concentration are marked in red. (b) The corresponding voltage profile.

We also assess the cycling stability of HZGM-42, wich is mainly determined by the volume changes during the Li charging/dischargeing process. We compare the fully Li-intercalated HZGM-42 with the pristine structure, and find that no bond-breaking occurs and the lattice changes along the *x*, *y* and *z* directions are only 0.3%, 0.2%, and 2.0% respectively. These changes are far less than the fracture strains shown in Fig. 2, comfirming that HZGM-42 retains its structural stability during lithiation/delithiation processes. With the small lattice changes, we obtain the toal volume expansion to be as low as 2.4%, which is much smaller than that of graphite (10%).[4] The ultra-low volume expansion can be attributed to the nanoporous nature of HZGM-42 that provides sufficient void space for Li-ion insertion. The low volume expansion of Li insertion and

the large fracture strain imply that HZGM-42 has a good cycling stability during lithiation/delithiation process when used as an anode material.

In addition, we find that a series of 3D graphene monoliths with different pore sizes can be generated by changing the width of the zigzag graphene nanoribbons. For instance, another hexagonal zigzag graphene monolith (HZGM) with same lattice symmetry as that of HZGM-42, containing 66 carbon atoms per primitive cell, called HZGM-66, is constructed. Its dynamic, thermal and mechanical stabilities are confirmed by following the same procedure (see Fig. S10 in the ESI for the details). HZGM-66 is also a semimetal with a Dirac linear dispersion near the Fermi level, as shown in Fig. S11e. Therefore, we further explore its potential for LIB anode material. The calculated diffusion barriers for similar paths (path I and Path II, as shown in Fig. S12) are 0.03 and 0.17 eV, respectively, close to those of HZGM-42. The maximum Li capacity is 676.4 mAh/g, which is even larger than that of HZGM-42 (647.7 mAh/g). The volume expansion is 3.0 % for the fully Li-intercalated structure (see Fig. S13), suggesting a good cycling stability of HZMG-66.

Conclusions

In summary, we predict a new 3D graphene monolith, HZGM-42, by integrating zigzag graphene nanoribbons with the sp^3-hybridized carbon chains as linkers. This material has the advantage of intrinsic high electrical coductivity and ordered porosity for Li-ion transport. By performing state-of-the-art theoretical calculations, we demonstrate that HZGM-42 is not only dynamically, thermally and mechanically stable, but also energetically more favorable than most of the previously identified 3D carbon allotropes.

Because of its unique atomic configuration, HZGM-42 exhibits exceptional properties including anisotropic elasticity, high specific ideal strength along the z direction, intrinsic Dirac nodal-line semimetallicity and anisotropic transport properties. Moreover, we examine the energetics and kinetics of Li-ion insertion and diffusion in HZGM-42, and the following conclusions can be drawn: (*i*) Li ions can be inserted into HZGM-42 stably without clustering; (*ii*) HZGM-42 possesses two remarkable 1D Li-ion diffusion paths and the migration energy barriers can reach quite low values, especially for Path I (0.02 eV). (*iii*) The maximum Li capacity of HZGM-42 is 637.7 mAh/g, corresponding to $LiC_{3.5}$, which is much higher than the commercially used graphite anode (372 mAh/g; LiC_6). (*iv*) Compared with the conventional graphite anode, HZGM-42 exhibits a much lower volume change (2.4%) during the Li insertion/removal process, indicating a good cycling stability. With all of these extraordinary characteristics, HZGM-42 shows a great potential as LIB anode material. Our study reveals the great potential of 3D graphene monoliths with intrinsic semi-metallicity and ordered pores to be applied as LIB anode material. We hope that these findings will motivate further theoretical and experimental efforts to find new semi-metallic 3D graphene monoliths for high-performance LIB anode materials. These results suggest that, compared to the currently used anode material in LIB, the new 3D graphene architecture exhibits superior properties.

Acknowledgements

References

1 S. Y. Hong, Y. Kim, Y. Park, A. Choi, N.-S. Choi and K. T. Lee, *Energy Environ. Sci.*, 2013, **6**, 2067-2081.
2 E. M. Erickson, C. Ghanty and D. Aurbach, *J. Phys. Chem. Lett.*, 2014, **5**, 3313-3324.
3 P. G. Bruce, S. A. Freunberger, L. J. Hardwick and J.-M. Tarascon, *Nature Mater.*, 2012, **11**, 19-29.
4 J. Liu, S. Wang and Q. Sun, *Proc. Natl. Acad. Sci.*, 2017, 201618051.
5 S. Goriparti, E. Miele, F. De Angelis, E. Di Fabrizio, R. P. Zaccaria and C. Capiglia, *J. Power Sources*, 2014, **257**, 421-443.
6 H. Li and H. Zhou, *Chem. Commun.*, 2012, **48**, 1201-1217.
7 L. Ji, Z. Lin, M. Alcoutlabi and X. Zhang, *Energy Environ. Sci.*, 2011, **4**, 2682-2699.
8 C. J. Meyers, S. D. Shah, S. C. Patel, R. M. Sneeringer, C. A. Bessel, N. R. Dollahon, R. A. Leising and E. S. Takeuchi, *J. Phys. Chem. B*, 2001, **105**, 2143-2152.
9 F. Cheng, Z. Tao, J. Liang and J. Chen, *Chem. Mater.*, 2007, **20**, 667-681.
10 A. D. Roberts, X. Li and H. Zhang, *Chem. Soc. Rev.*, 2014, **43**, 4341-4356.
11 X. Deng, B. Zhao, Y. Sha, Y. Zhu, X. Xu and Z. Shao, *ChemElectroChem*, 2016, **3**, 698-703.
12 V. Etacheri, C. Wang, M. J. O'Connell, C. K. Chan and V. G. Pol, *J. Mater. Chem. A*, 2015, **3**, 9861-9868.
13 J. Hou, C. Cao, F. Idrees and X. Ma, *ACS Nano*, 2015, **9**, 2556-2564.
14 K. Umemoto, S. Saito, S. Berber and D. Tománek, *Phys. Rev. B*, 2001, **64**, 193409.
15 T. Kawai, S. Okada, Y. Miyamoto and A. Oshiyama, *Phys. Rev. B*, 2005, **72**, 035428.
16 Z. Zhao, B. Xu, L.-M. Wang, X.-F. Zhou, J. He, Z. Liu, H.-T. Wang and Y. Tian, *ACS Nano*, 2011, **5**, 7226-7234.
17 Z. Zhu, Z. G. Fthenakis, J. Guan and D. Tománek, *Phys. Rev. Lett.*, 2014, **112**, 026803.
18 X. Jiang, J. Zhao, Y. L. Li and R. Ahuja, *Adv. Funct. Mater.*, 2013, **23**, 5846-5853.
19 N. V. Krainyukova and E. N. Zubarev, *Phys. Rev. Lett.*, 2016, **116**, 055501.
20 Y. Gao, Y. Chen, C. Zhong, Z. Zhang, Y. Xie and S. Zhang, *Nanoscale*, 2016, **8**,

12863-12868.

21 G. Kresse and J. Furthmüller, *Phys. Rev. B*, 1996, **54**, 11169.

22 J. P. Perdew, K Burke, M. Ernzerhof . *Phys. Rev. Lett.* **1996,** 77, 3865.

23 P. E. Blöchl, *Phys. Rev. B*, 1994, **50**, 17953.

24 J. Heyd, G. E. Scuseria and M. Ernzerhof, *J. Chem. Phys.*, 2003, **118**, 8207-8215.

25 H. J. Monkhorst and J. D. Pack, *Phys. Rev. B,* 1976, **13**, 5188.

26 S. Nosé, *J. Chem. Phys.*, 1984, **81**, 511-519.

27 X. Gonze, *Phys. Rev. B*, 1997, **55**, 10337-10354.

28 A. Togo, F. Oba and I. Tanaka, *Phys. Rev. B*, 2008, **78**, 134106.

29 G. Henkelman, B. P. Uberuaga and H. Jónsson, *J. Chem. Phys.*, 2000, **113**, 9901-9904.

30 G. Henkelman and H. Jónsson, *J. Chem. Phys.*, 2000, **113**, 9978-9985.

31 S. Grimme, *J. Comput. Chem.*, 2006, **27**, 1787-1799.

32 Y. Jing, Z. Zhou, C. R. Cabrera and Z. Chen, *J. Phys. Chem. C.*, 2013, **117**, 25409-25413.

33 Q. Tang, Z. Zhou and P. Shen, *J. Am. Chem. Soc.*, 2012, **134**, 16909-16916.

34 E. Lee and K. A. Persson, *Nano Lett.*, 2012, **12**, 4624-4628.

35 S. Yamanaka, A. Kubo, K. Inumaru, K. Komaguchi, N. Kini, T. Inoue and T. Irifune, *Phys. Rev. Lett.*, 2006, **96**, 076602.

36 K. M. Merz Jr, R. Hoffmann and A. T. Balaban, *J. Am. Chem. Soc.*, 1987, **109**, 6742-6751.

37 M. J. Bucknum and R. Hoffmann, *J. Am. Chem. Soc.*, 1994, **116**, 11456-11464.

38 S. Zhang, Q. Wang, X. Chen and P. Jena, *Proc. Natl. Acad. Sci.*, 2013, **110**, 18809-18813.

39 K. Umemoto, R. M. Wentzcovitch, S. Saito and T. Miyake, *Phys. Rev. Lett.*, 2010, **104**, 125504.

40 P. A. Schultz, K. Leung and E. Stechel, *Phys. Rev. B*, 1999, **59**, 733.

41 Y. Liu, X. Jiang, J. Fu and J. Zhao, *Carbon*, 2018, **126**, 601-610.

42 Y. Chen, Y. Xie, S. A. Yang, H. Pan, F. Zhang, M. L. Cohen and S. Zhang, *Nano Lett.*, 2015, **15**, 6974-6978.

43 V. A. Blatov and D. M. Proserpio, *Acta Crystallogr. Sect. A*, 2009, **65**, 202-212.

44 J.-T. Wang, H. Weng, S. Nie, Z. Fang, Y. Kawazoe and C. Chen, *Phys. Rev. Lett.*, 2016, **116**, 195501.

45 J. Liu, T. Zhao, S. Zhang and Q. Wang, *Nano Energy*, 2017, **38**, 263-270.

46 Z. Pang, X. Gu, Y. Wei, R. Yang and M. S. Dresselhaus, *Nano Lett.*, 2016, **17**, 179-185.

47 Y. Zhang, H. Sun and C. Chen, *Phys. Rev. Lett.*, 2004, **93**, 195504.

48 Y. Kim, B. J. Wieder, C. Kane and A. M. Rappe, *Phys. Rev. Lett.*, 2015, **115**, 036806.

49 R. Li, H. Ma, X. Cheng, S. Wang, D. Li, Z. Zhang, Y. Li and X.-Q. Chen, *Phys. Rev. Lett.*, 2016, **117**, 096401.

50 R. Yu, H. Weng, Z. Fang, X. Dai and X. Hu, *Phys. Rev. Lett.*, 2015, **115**, 036807.

51 J. Lahiri, Y. Lin, P. Bozkurt, I. I. Oleynik and M. Batzill, *Nat. Nanotech.*, 2010, **5**, 326-329.

52 W. Tang, E. Sanville and G. Henkelman, *J. Phys. Condens. Matter*, 2009, **21**, 084204.

53 K. Nishidate and M. Hasegawa, *Phys. Rev. B*, 2005, **71**, 245418.

54 K. Persson, V. A. Sethuraman, L. J. Hardwick, Y. Hinuma, Y. S. Meng, A. van der Ven, V. Srinivasan, R. Kostecki and G. Ceder, *J. Phys. Chem. Lett.*, 2010, **1**, 1176-1180.

55 W. Li, Y. Yang, G. Zhang and Y.-W. Zhang, *Nano Lett.*, 2015, **15**, 1691-1697.

56 J. Liu, S. Wang, Y. Qie, C. Zhang and Q. Sun, *Phys. Rev. Mater.*, 2018, **2**, 025403.

57 D. Çakır, C. Sevik, O. Gülseren and F. M. Peeters, *J. Mater. Chem. A*, 2016, **4**, 6029-6035.

58 M. Aydinol, A. Kohan, G. Ceder, K. Cho and J. Joannopoulos, *Phys. Rev. B*, 1997, **56**, 1354.

59 Z. Yang, D. Choi, S. Kerisit, K. M. Rosso, D. Wang, J. Zhang, G. Graff and J. Liu, *J. Power Sources*, 2009, **192**, 588-598.

39x27mm (300 x 300 DPI)